Polymer/Perovskite-Type Nanoparticle Multilayers with Multielectric Properties Prepared from Ligand Addition-Induced Layer-by-Layer Assembly

Younghoon Kim,[†,§] Kyungyun Kook,[†,§] Sun Kak Hwang,[‡] Cheolmin Park,[‡] and Jinhan Cho[†,*]

[†]Department of Chemical & Biological Engineering, Korea University, Anam-dong, Seongbuk-gu, Seoul 136-713, South Korea and [‡]Department of Materials Science and Engineering, Yonsei University, 50 Yonsei-ro, Seodaemun-gu, Seoul 120-749, South Korea. [§]Y. Kim and K. Kook contributed equally to this work.

ABSTRACT We introduce an adsorption mechanism for a layer-by-layer (LbL) assembly (*i.e.*, a *ligand addition-induced LbL assembly*) and demonstrate that the (polymer/perovskite nanoparticle (NP))$_n$ nanocomposite films based on the ligand addition LbL exhibit ferroelectric and resistive switching properties. Oleic acid (OA)-stabilized $BaTiO_3$ NPs (OA-BTO NPs) with a size of approximately 8 nm were LbL-assembled with amine-functionalized dendrimers (NH_2-dendrimers) using the high affinity between NH_2 moieties and Ti ions. The ferroelectric properties of the (NH_2-dendrimer/OA-BTO NP)$_n$ multilayers were generated by the Ti disorder in the OA-BTO NP unit cell despite the use of sub-10 nm OA-BTO NPs (*i.e.*, OA-BTO NPs), which are near the critical size for ferroelectric properties. Additionally, the (NH_2-dendrimer/OA-BTO NP)$_n$ multilayers sandwiched between the bottom (platinum) and top (silver or tungsten) electrodes exhibited a resistive switching memory at a relatively low operating voltage below 2 V with a switching speed of approximately 100 ns and an ON/OFF current ratio of approximately 10^4. Furthermore, the ferroelectric and resistive switching properties could be further improved by controlling the bilayer number (n). We believe that our approach can provide a basis for designing and exploiting multifunctional memory electronics based on a variety of perovskite NPs with ferroelectric properties.

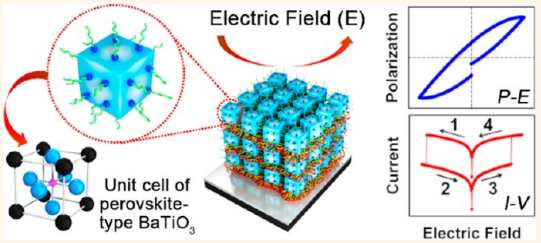

KEYWORDS: layer-by-layer assembly · multilayers · $BaTiO_3$ nanoparticle · ferroelectric · nonvolatile memory

Perovskite-type materials with unique electronic properties have attracted significant attention due to their scientific importance and widespread applications in microelectronics and electro- and nonlinear optics.[1−8] Barium titanate ($BaTiO_3$) (BTO), which is composed of BaO_{12} cuboctahedra and TiO_6 octahedra, is among the most technologically promising perovskite-type ceramics due to its ferroelectric, pyroelectric, piezoelectric, dielectric, and resistive switching properties, which are useful in a variety of potential applications such as ceramic capacitors, piezoelectric transducers, thermistors, waveguide modulators, pressure transducers, and nonvolatile memory devices.[9−16]

Recently, the increased interest in nanoscale phenomena and nanoelectronics has given rise to a great deal of research into BTO nanoparticles (NPs) prepared using a variety of solution-based methodologies. Although many attempts have been made at synthesizing monodisperse BTO NPs with size-dependent ferroelectric properties,[17−22] the development of high-quality (*i.e.*, uniform size and high crystallinity) BTO NPs below 50 nm has met with limited success, resulting in no experimental consensus on the critical size at which ferroelectricity is suppressed. Recently, aided by the successful synthesis of well-defined BTO NPs with controlled size and highly crystalline structures,[23,24] a sub-10 nm BTO as an individual NP has reportedly displayed ferroelectric behavior.[24] However, these BTO NPs cannot be directly applied to the aforementioned practical devices due to their poor processability.

To resolve these issues, BTO NPs have been blended with polymer matrixes *via* mechanical blending, solution mixing, *in situ* polymerization, and *in situ* NP synthesis.[12−15,25,26] These NPs have been used as a form of

* Address correspondence to jinhan71@korea.ac.kr.

Received for review November 19, 2013 and accepted February 23, 2014.

Published online February 24, 2014
10.1021/nn405988d

organic–inorganic nanocomposite films with a single-layer structure. For example, Kim *et al*. reported that combining high-permittivity BTO NPs and a polymer host could provide nanocomposite films with high permittivity and high dielectric strength to allow for solution processing.[12] However, in most cases, the perovskite-type NPs dispersed within polymer matrixes lead to aggregation and phase segregation over large distances to the detriment of the electrical properties of the nanocomposites. Additionally, relatively large sized (>100 nm) BTO NPs have been used to prepare polymer–BTO NP nanocomposite films. However, the use of these materials as an ultrathin electrically active layer (<100 nm thick), such as a nonvolatile memory layer or high-dielectric-constant layer in organic thin-film transistors, is restricted. Furthermore, to our knowledge, organic–inorganic nanocomposite films based on sub-10 nm BTO NPs have not been reported to date.

To fabricate nanocomposite films, the layer-by-layer (LbL) assembly method based on the dipping process demonstrates potential as the most versatile and offers the possibility of preparing nanocomposite films with tailored electrical, mechanical, or optical properties.[27−50] Although a variety of materials ranging from biomaterials to inorganic NPs such as metal and binary metal oxide NPs have been successfully utilized in the LbL-assembled nanocomposite films *via* complementary interactions (electrostatic interactions,[27,28,30−32] hydrogen-bonding,[31] click chemistry,[33] silanization,[34] oxime bonding,[35] thiol–metal interactions,[36] nucleophilic substitution reactions,[37−39] ligand exchange reactions,[41,42] photo-cross-linking,[43] multivalent coordination bonding,[44] *etc*.), the well-defined perovskite-type NPs dispersed in nonpolar solvents have not been directly applied in LbL-assembled nanocomposite films. Therefore, preparing BTO NPs from fatty acid stabilizers that are homogeneously and uniformly embedded within ultrathin LbL-assembled films remains a major challenge; furthermore, their inherent properties such as their ferroelectric and/or resistive bipolar switching should be enhanced and adjusted through the facile control of the quantity adsorbed in the lateral and vertical dimensions.

Herein, we demonstrate that the nanocomposite multilayer films based on highly monodisperse cube-like BTO NPs of approximately 8 nm can be successfully generated through a unique LbL-assembly adsorption mechanism (*i.e*., *ligand addition-induced LbL assembly*) in an organic solvent. These LbL films display ferroelectric switching properties with reversible spontaneous polarization and oxygen-deficiency-induced resistive switching memory. In addition, these film devices were prepared and operated at room temperature. For this study, the synthetic procedure reported by Dang *et al*. (for the synthesis of BTO NPs ranging from 20 to 30 nm) was modified to prepare the oleic acid (OA)-BTO NPs through a hydrothermal process.[51] The OA-BTO NPs dispersed in toluene were LbL-assembled with NH_2-dendrimers in ethanol using the additional covalent bonding between NH_2 groups and Ti^{4+} ions without any OA ligand exchange. The conventional adsorption behavior reported to date for LbL-assembled polymer/inorganic NP multilayers is induced by the high affinity (*i.e*., electrostatic, covalent, or hydrogen bonding) or ligand exchange[42] between the polymer and the stabilizers of the inorganic NPs as previously described. However, to our knowledge, the adsorption behavior based on ligand addition in the LbL assembly for hydrophobic perovskite NPs with well-defined crystallinity has not yet been reported.

Our approach has another important advantage in that multilayer structures can significantly increase the number density of ferroelectric elements in the lateral and vertical dimensions, allowing tailored nanostructures that can enhance the ferroelectric properties by increasing the bilayer number. Furthermore, the $(NH_2$-dendrimer/OA-BTO NP$)_n$ films exhibited a nonvolatile resistive switching memory with a high ON/OFF current ratio of $\sim 10^4$, a low operating voltage (<2 V), and good retention stability comparable to that of a conventional transition metal oxide device fabricated *via* vacuum deposition with subsequent temperature annealing (>200 °C). Recently, the Advincula group reported that nanometer-scale charging in LbL films based on conjugated polymers can provide a write–read device using current-sensing atomic force microscopy.[52] More recently, the Pal group reported that the electrostatic assembled multilayers composed of CdSe quantum dots can display electrical bistability with the ON/OFF current ratio of $\sim 10^1$.[53] As another example, we reported that LbL multilayers containing Fe_3O_4 NPs exhibit a resistive switching memory performance of $\sim 10^2$.[38,40] It should be here noted that the previously reported results have been obtained from the traditional electrostatic, nucleophilic substitution reaction-induced, and the ligand exchange-induced LbL assembly, which are totally different from ligand addition-induced LbL assembly shown in our study. Furthermore, to our knowledge, the LbL-assembled films with ferroelectric properties have been never reported to date.

This study reports the first successful preparation of ferroelectric and resistive switching films based on sub-10 nm BTO NPs (*i.e*., OA-BTO NPs) *via* ligand addition-induced LbL assembly. We believe that our strategy can provide a basis for developing and designing a variety of functional nanocomposite films using other perovskite-type NPs, allowing us to explore novel technological applications.

RESULTS AND DISCUSSION

Cube-like 8 nm OA-BTO NPs that are highly dispersible in nonpolar organic solvents were successfully synthesized by controlling the molar ratios between

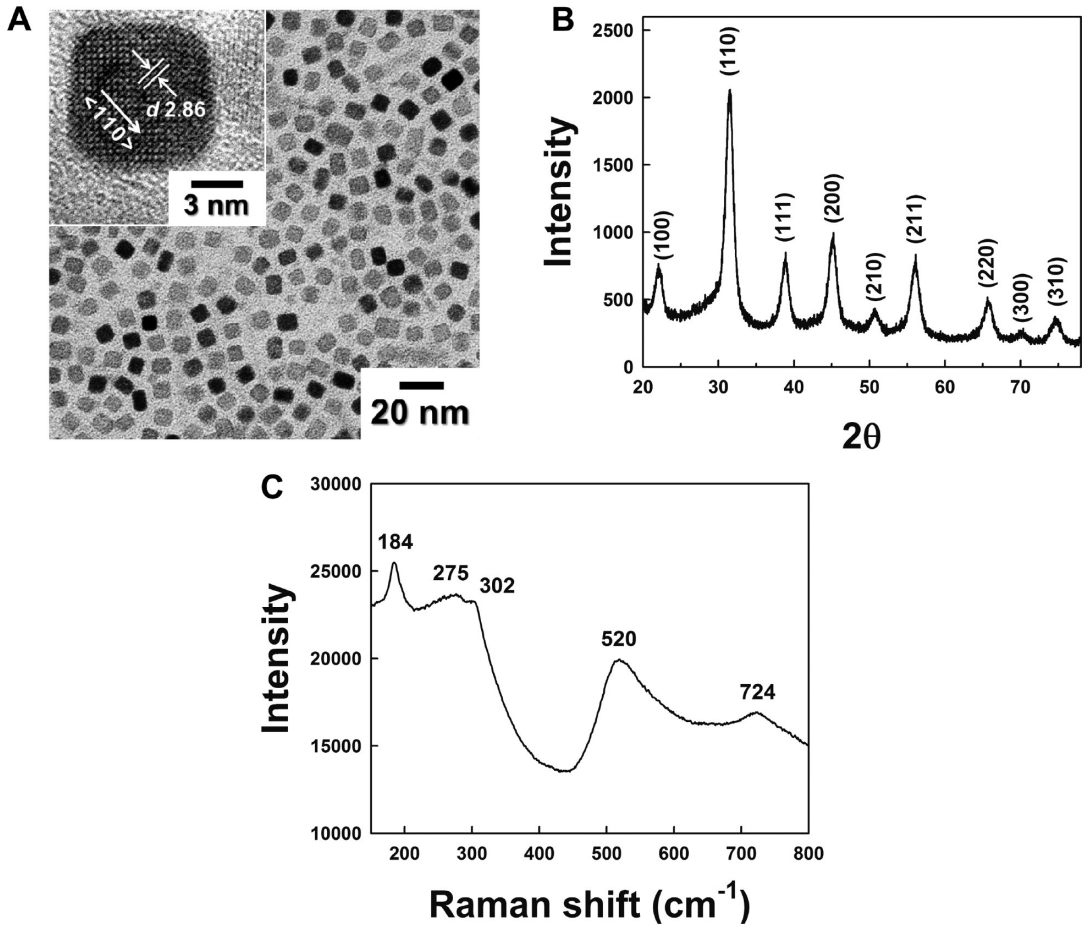

Figure 1. (A) HR-TEM image of the approximately 8 ± 0.7 nm OA-BTO NPs. (B) XRD pattern and (C) Raman spectrum of the OA-BTO NP powder.

the water-soluble bis(ammonium lactate) titanium dihydroxide, barium hydroxide, *tert*-butylamine, and oleic acid *via* a hydrothermal process (the detailed synthetic procedure is provided in the Methods section). Figure 1A provides an HR-TEM image of highly monodisperse OA-BTO NPs with sizes of 8.0 ± 0.7 nm and a lattice image of a OA-BTO NP effectively viewed along the [110] projection. The material appears to have a single crystal domain. As indicated in the size distribution histogram, which is evaluated using the HR-TEM image, the size of the OA-BTO NPs is highly monodisperse (see Supporting Information, Figure S1). The crystal structure of the OA-BTO NPs was further characterized *via* X-ray diffraction (XRD). As presented in Figure 1B, the XRD pattern of the OA-BTO NPs exhibited a series of well-defined Bragg reflections that can be indexed into a pseudocubic lattice, suggesting that the sample is single-phase and highly crystalline. Additionally, no XRD patterns originating from a by-product such as $BaCO_3$ were observed.

Figure 1C presents the Raman spectrum of OA-BTO NPs recorded at room temperature. The spectrum exhibits weak peaks at 275 and 302 cm^{-1}, two strong peaks at 184 and 520 cm^{-1}, and a broad peak at 724 cm^{-1}. The OA-BTO NPs with a paraelectric cubic phase (space group *Pm*3*m*) are reportedly Raman inactive due to the isotropic distribution of electrostatic forces (O_h group symmetry) around the Ti^{4+} ions within each TiO_6 octahedron.[23,54−56] However, the Raman spectrum of the OA-BTO NPs with a tetragonal ferroelectric phase demonstrates a splitting of the four degenerate $3F_{1u} + F_{2u}$ modes into eight Raman-active transverse (TO) and longitudinal (LO) phonons that control the anomalous Raman scattering. Therefore, the five bands at 184, 275, 302, 520, and 724 cm^{-1} are assigned to the A_1(LO), A_1(TO), B_1 + E(TO + LO), E(TO) + A_1(TO), and A_1(LO) + E(LO) modes, respectively, suggesting that the OA-BTO NPs exhibit a noncentrosymmetric tetragonal phase with the characteristics of titanium disorder in the unit cell at room temperature.

On the basis of these results, NH_2-dendrimers and OA-BTO NPs were alternately deposited onto the planar substrates to fabricate the OA-BTO NP-based nanocomposite films. Recently, our group reported that OA-Ag or OA-Fe_3O_4 NPs can be LbL-assembled with NH_2-dendrimers *via* a direct ligand exchange reaction between OA and NH_2 groups during deposition.[40,41] However, the adsorption behavior between the OA-BTO NP and the NH_2-dendrimer was based on the additional coordination bonding between the NH_2

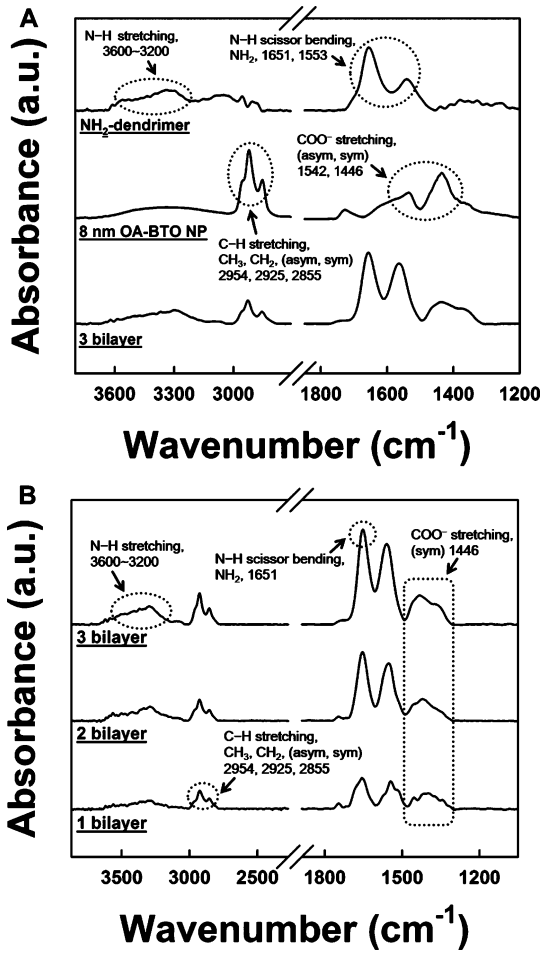

Figure 2. (A) ATR-FT-IR spectra of the NH_2-dendrimer, OA-BTO NP, and (NH_2-dendrimer/OA-BTO NP)$_3$ multilayer. (B) ATR-FT-IR spectra of the (NH_2-dendrimer/OA-BTO NP)$_{n=1,2,3}$ multilayers as a function of the bilayer number (n).

groups and the Ti^{4+} ions, not on the replacement of the OA ligands. This adsorption mechanism was confirmed using Fourier-transform infrared spectroscopy (FT-IR).

We first examined the FT-IR spectra of pure NH_2 dendrimers, OA-BTO NPs, and (NH_2-dendrimer/OA-BTO NP)$_3$ multilayer (Figure 2A). The N−H stretching (3200−3600 cm^{-1}) and N−H scissor bending (1553 and 1651 cm^{-1}) peaks contributed to the primary amine groups of the NH_2-dendrimers. Additionally, the C−H stretching (2855, 2925, and 2954 cm^{-1}) and C═O stretching (1711 cm^{-1}) peaks originate from the long aliphatic chains and carboxylic acid (*i.e.*, COOH) groups of the pure OA ligands, respectively (see Supporting Information, Figure S2). However, when the OA ligands are adsorbed onto the surface of the OA-BTO NPs, the carboxylic acid groups of the OA ligands are bonded to the OA-BTO NPs in the form of carboxylate (*i.e.*, COO^-) ions. This phenomenon was confirmed from the COO^- stretching (1446 and 1542 cm^{-1}) peaks present in the FT-IR spectrum of the OA-BTO NPs. The carboxylate group of OA ligands is reportedly chemically bonded to the alkali metal ions on the surface of the BTO NPs.[49] That is, the OA ligands are primarily adsorbed onto the crystal face with a high density of Ba ions because all six-coordinate positions of the Ti ion are occupied by hydroxyl groups in the OA-BTO NP system.[17]

Furthermore, we investigated the absorption peak traces of the transmission and attenuated total reflection (ATR)-FT-IR spectra of the (NH_2-dendrimer/OA-BTO NP)$_n$ multilayers as a function of the bilayer number (n). As shown in Figure 2B, the COO^- stretching (1446 and 1542 cm^{-1}) peaks and C−H stretching (2855, 2925, and 2954 cm^{-1}) peaks of the long aliphatic chain of OA ligands bound to the OA-BTO NPs grew in intensity as the bilayer number (n) increased from 1 to 3. The N−H absorption peak intensities (*i.e.*, stretching in the range 3200−3600 cm^{-1} and bending modes at 1651 cm^{-1}) of the NH_2-dendrimers also increased gradually with those of the OA ligands. Therefore, these results indicate that the adsorption mechanism between the NH_2-dendrimer and OA-BTO NP is based on the ligand addition reaction of the NH_2 dendrimer onto the OA-BTO NP.

This ligand addition reaction can be more evidently confirmed by the comparison of ATR-FT-IR spectra between NH_2-dendrimer/OA-Ag NP/NH_2-dendrimer and NH_2-dendrimer/OA-BTO NP/NH_2-dendrimer. It was reported that the LbL assembly of (NH_2-dendrimer/OA-Ag NP)$_n$ multilayers is based on the ligand-exchange reaction.[41,42] Therefore, in the case where NH_2-dendrimers are further adsorbing onto the outermost OA-Ag NP layer coated film (*i.e.*, NH_2-dendrimer/OA-Ag NP/NH_2-dendrimer), the absorption peaks (*i.e.*, the long aliphatic C−H stretching (2855, 2925, and 2925 and 2954 cm^{-1}) and COO^- stretching (1453 and 1400 cm^{-1})) originating from the OA ligands bound to the surface of Ag NPs were almost completely replaced by NH_2-dendrimer after about 30 min (see Supporting Information, Figure S3). On the other hand, in the case of a (NH_2-dendrimer/OA-BTO NP/NH_2-dendrimer) film, the absorption peaks and intensities of OA ligands remained unchanged even after 30 min. Therefore, our results indicate that the adsorption mechanism of LbL-assembled (NH_2-dendrimer/OA-BTO NP)$_n$ multilayers is mainly based on a ligand addition reaction.

The site at which the OA-BTO NPs adsorb onto the NH_2-dendrimer layer and the chemical states of the OA-BTO NPs were investigated *via* X-ray photoelectron spectroscopy (XPS) (Figure 3). A Ba $3d_{5/2}$ binding energy of 779 eV was measured for the pristine OA-BTO NPs, which coincided with that of the OA-BTO NP-based multilayers. The Ti $2p_{3/2}$ XPS peak of the pristine OA-BTO NPs was resolved into two spin−orbit components, which were assigned to Ti^{4+} (458.4 eV) and Ti^{3+} (457.6 eV). Additionally, the Ti^{3+} spectrum indicated the presence of an oxygen-deficient state within the NPs that can be used as a positively charged carrier in resistive switching memory devices

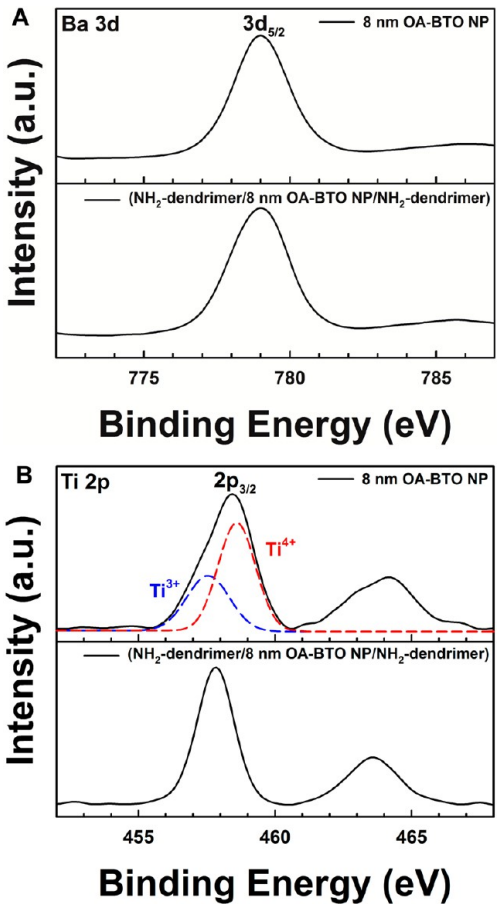

Figure 3. XPS spectra of (A) Ba 3d and (B) Ti 2p collected from the OA-BTO NPs and NH_2-dendrimer-encapsulated films [*i.e.*, (NH_2-dendrimer/OA-BTO NP/NH_2-dendrimer) multilayer].

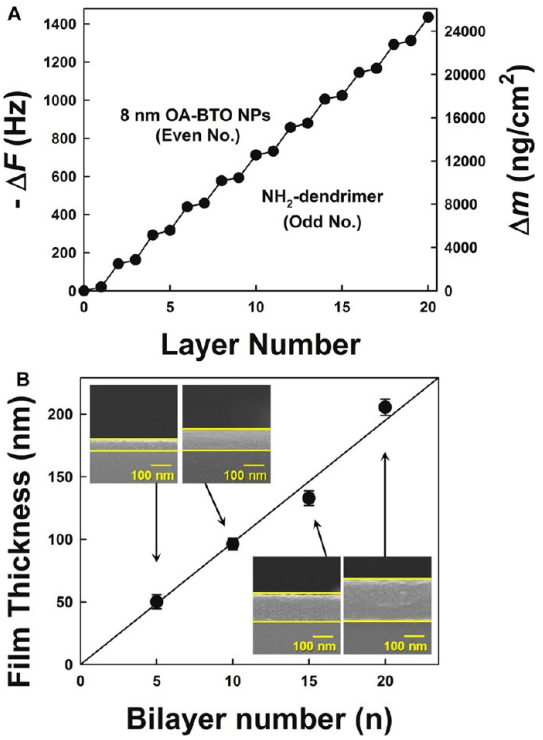

Figure 4. (A) Frequency and mass change of the NH_2-dendrimer/OA-BTO NPs multilayers as a function of the layer number. (B) Total film thicknesses of the (NH_2-dendrimer/OA-BTO NP)$_{n=5,10,15,20}$ multilayers measured from the cross-sectional SEM images.

(a detailed explanation of which will be provided in a subsequent section).[56−58] However, when NH_2 dendrimers were adsorbed onto the OA-BTO NP surfaces, the Ti $2p_{3/2}$ peak in the XPS spectrum shifted from 458.3 to 457.7 eV.

These phenomena are supported by previous reports, which indicated that the binding between titanium and nitrogen causes a strong shift in the principle Ti $2p_{3/2}$ peak toward lower energy.[59,60] Therefore, one can reasonably conclude that the $-NH_2$ groups of the NH_2-dendrimers are chemically bonded to the Ti ions of the OA-BTO NPs. This adsorption phenomenon demonstrated in our system clearly differs from the previously reported adsorption behavior based on the ligand-exchange reaction in which the initial ligands bound to metal or metal oxide NPs (*e.g.*, OA-Ag NP, TOABr-Au NP, or OA-Fe_3O_4) are replaced with ligands containing higher affinity groups: the formation of the (NH_2-dendrimer/OA-BTO NP)$_n$ films is based on a ligand addition-induced LbL assembly.

Given these results, the quantity of NH_2-dendrimer and OA-BTO NP adsorbed onto the multilayer films was quantified *via* quartz crystal microgravimetry (Figure 4A). Measuring the frequency changes (ΔF) from which the mass changes (Δm) were calculated for the alternating deposition of NH_2-dendrimer and OA-BTO NP yielded $-\Delta F$ values of 20 ± 4 Hz ($\Delta m \approx 353$ ng·cm^{-2}) and 124 ± 6 Hz ($\Delta m \approx 2191$ ng·cm^{-2}), respectively. Given that the density and volume of an 8 nm cube-like OA-BTO NP are approximately 6.02 g·cm^{-3} and 5.12 × 10^{-19} cm^{-3}, respectively, the number density and packing density of the OA-BTO NP were calculated at approximately 7.1 × 10^{11} cm^{-2} and 45.5%, respectively. Although Kim *et al.* reported the preparation of ferroelectric islands with an ultra-high-density array using block copolymer micelles, their number density is below approximately 1 × 10^9 cm^{-2}.[61] On the other hand, the successive spin-coated multilayer films using OA-BTO NP without the aid of NH_2-dendrimer layers could not be formed due to the absence of complementary interactions between each NP (see Supporting Information, Figure S4).

Additionally, we investigated the thickness of the nanocomposite films as a function of the bilayer number using cross-sectional scanning electron microscopy (SEM). The total film thicknesses of the (NH_2-dendrimer/OA-BTO NP)$_{n=5,10,15,20}$ multilayers were measured to be 50 ± 1.9 nm for n = 5, 98 ± 2.1 nm for n = 10, 139 ± 2.4 nm for n = 15, and 204 ± 2.8 nm for n = 20 (Figure 4B). The surfaces of multilayer films were highly uniform and smooth with a low root-mean-square

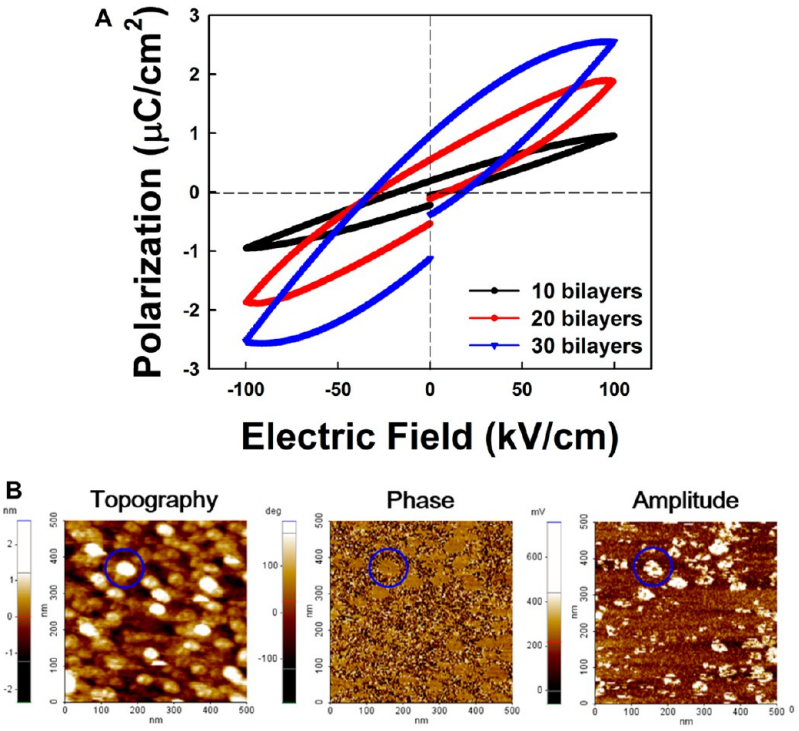

Figure 5. (A) Polarization-applied electric field (P—E) curves for the (NH_2-dendrimer/OA-BTO NP)$_{n=10,20,30}$ multilayers. (B) Topographic, phase, and amplitude images from the dynamic-contact electrostatic force microscopy (DC-EFM) for the OA-BTO NPs on a Pt-coated substrate.

(RMS) surface roughness. In the case of five-bilayered film, the RMS surface roughness was measured to be approximately 1.16 nm in a scan area of 1 μm × 1 μm. Additionally, the surface roughnesses of the (NH_2-dendrimer/OA-BTO NP)$_{n=5,10,15,20}$ multilayers in the larger scan area of 10 μm × 10 μm did not exceed 3 nm. Furthermore, the AFM image of (NH_2-dendrimer/OA-BTO NP)$_{10}$ measured from a 20 μm × 20 μm scan area clearly showed the homogeneity of the film. These results imply that ligand addition-induced LbL assembly can successfully generate an extremely smooth surface and vertical growth in OA-perovskite NP multilayers in organic media (see Supporting Information, Figure S5).

Considering that perovskite-type materials such as BTO NPs have unique optical properties such as second-harmonic generation[62] as well as electro-optical properties,[63] the film transparency is significantly important for the preparation of potential electronic and/or optical applications. Therefore, we investigated the light transmission of OA-BTO NP-based multilayer films. The 204-nm-thick (NH_2-dendrimer/OA-BTO NP)$_{20}$ nanocomposite films were highly transparent with light transmission of 92.7% at a wavelength of 600 nm (see Supporting Information, Figure S6). It should be noted that the conventional BTO nanocomposite films reported to date cause a high degree of light scattering due to the use of BTO NPs larger than 100 nm and the poor dispersion of BTO NPs within films and, thus, are opaque.[64] Therefore, our LbL-assembled nanocomposite films show a high degree of transparency due to the use of OA-BTO NPs and good dispersion within the film.

Given these results, we investigated the ferroelectric switching properties of (NH_2-dendrimer/OA-BTO NP)$_n$ multilayers at a frequency of 1 kHz. The approximately 98-nm-thick 10-bilayered film displayed typical ferroelectric polarization—electric field (P—E) hysteresis loops with a remnant polarization (P_r) of approximately 0.19 $\mu C \cdot cm^{-2}$ and a coercive field (E_c) of 8.2 $kV \cdot cm^{-1}$ under a 100 $kV \cdot cm^{-1}$ applied electric field (Figure 5A). By increasing the bilayer number (n) from 10 to 30, the P_r and E_c obtained from the P—E multilayer loop increased to 0.95 $\mu C \cdot cm^{-2}$ and 19 $kV \cdot cm^{-1}$, respectively. Although the P_r value of bulk BTO ceramics was reportedly measured at approximately 8 $\mu C \cdot cm^{-2}$,[65] the conventional nanocomposite films composed of nanosized BTO particles (>20 nm) and a polymer exhibited a low P_r of 0.4 $\mu C \cdot cm^{-2}$ despite the use of a thick film (>100 μm) and a maximized electric field of 600 $kV \cdot cm^{-1}$.[64] Additionally, given that the ferroelectricity (*i.e.*, P_r) is degraded when the size of the BTO NPs is reduced due to an increase in the depolarization field (E_d) within the BTO NPs,[24,66] the 300-nm-thick nanocomposite multilayers (*i.e.*, the 30-bilayered film) composed of OA-BTO NPs exhibit good ferroelectric switching behavior. Our results also imply that the ferroelectric switching behavior can be further enhanced by adjusting the bilayer number.[67]

For clarification, the fact that the ferroelectric properties of multilayer films originated from OA-BTO NPs,

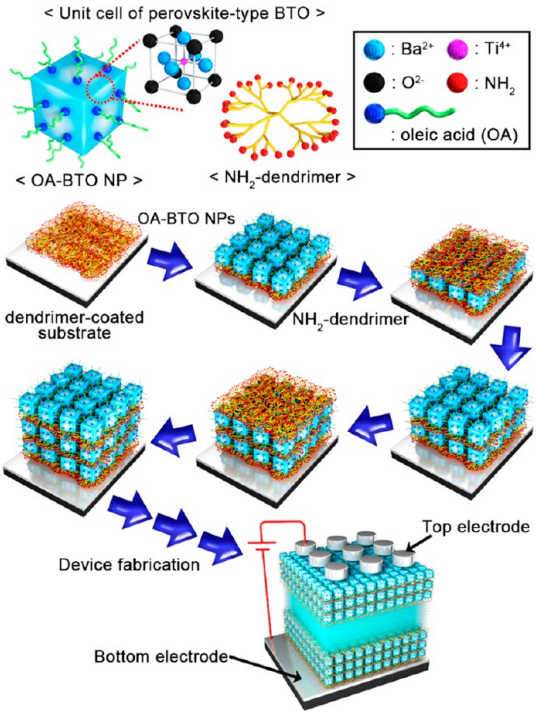

Scheme 1. Schematic diagram of the NH_2-dendrimer/OA-BTO NPs multilayer-based nonvolatile memory devices.

the induced rearrangements of the ferroelectric domain in the OA-BTO NPs were investigated *via* dynamic-contact electrostatic force microscopy (DC-EFM) using a lock-in amplifier.[19,61,68] First, the OA-BTO NPs spin-coated onto the Pt-coated substrate without a NH_2-dendrimer layer were poled using a positive dc bias (5 V) applied to the DC-EFM tip. Following the poling process, the topography, phase, and amplitude images were obtained *via* DC-EFM using 17 kHz ac voltage with a 1.5 V amplitude in contact mode. As depicted in Figure 5B, the bright regions of phase image indicate that the domain of the OA-BTO NPs confirmed in the topographic image was polarized in a downward direction on the substrate by the poling process. In addition, the polarization of the OA-BTO NPs could be more clearly confirmed by an amplitude image indicating the polarization strength, irrespective of the domain direction. Additionally, the blue circles indicate the same position for each topographic, phase, and amplitude image. Therefore, these images demonstrate that the respective OA-BTO NPs have ferroelectric domains indicated by the distorted Ti ions of OA-BTO NPs as already described for Figure 1C.

We prepared bipolar resistive switching memory devices[58,69−72] composed of (NH_2-dendrimer/OA-BTO NP)$_{n=2,3,5}$ multilayers deposited onto platinum (Pt)-coated Si substrates and Ag top electrodes with diameters of 50 μm as indicated in Scheme 1. The electrical measurements of the nonvolatile memory cells were performed using an applied dc voltage under atmospheric conditions. All voltages were applied to the top electrode, while the bottom electrode was grounded. In a typical bipolar switching measurement, which depends on the voltage polarity, the voltage sweeps from 0 V to −2.0 V and back to +2.0 V after an initial electroforming process (for a conductive path within the multilayers) at approximately 4.7 V with limited current compliance up to 100 mA (see Supporting Information, Figure S7). The high-current state (the "ON" state) formed from 0 V to −2.0 V was suddenly converted to a low-current state (the RESET process for the "OFF" state) at −1.8 V when the reverse voltage polarity was applied to the (NH_2-dendrimer/OA-BTO NP)$_{n=2,3,5}$ multilayered devices. This low-current state (the "OFF" state) was maintained from −2.0 V to +2.0 V and then converted to the high-current state at +1.5 V (the SET process for the "ON" state). Additionally, an increase in the bilayer number (*i.e.*, an increased multilayer thickness) lowered the OFF current level because the increased film thickness decreased the electric field (Figure 6A). Thus, the ON/OFF current ratio of these devices increased to approximately 10^4. Although the OA-BTO NP films for the preparation of resistive switching memory devices could be prepared by the single-step spin-coating process (or simple-casted coating) through the control of the concentration of the OA-BTO NP solution and the spinning speed (see Supporting Information, Table S1), these processes have much difficulty in exactly controlling the thickness of OA-BTO films. Additionally, the surface of the simple-casted or single-step spin-coated OA-BTO NP films was highly porous and rough compared to that of LbL-assembled nanocomposite films (see Supporting Information, Figure S8). As a result, these film devices did not exhibit the resistive switching memory performance due to an outbreak of short-circuit current (see Supporting Information, Figure S9).

For examining the stability of the bipolar resistive switching properties, cycling and retention time tests were carried out on the five-bilayered NH_2-dendrimer/OA-BTO NP devices to measure their electrical stability in the ON and OFF states (Figure 6B and C). In these cases, highly stable ON and OFF states were retained during the repeated cycling tests of approximately 200 cycles with a fast switching speed of 100 ns and a time period of 10^5 s under atmospheric conditions. To understand the conducting behavior of the NH_2-dendrimer/OA-BTO NP film devices, the $I-V$ relationship during the positive voltage sweep was further investigated using a log−log scale (Figure 6D). The $I-V$ characteristics obtained from the ON state displayed ohmic behavior with a slope of approximately 1.10, which shows the formation of conductive channels within the multilayer films during the SET process. On the other hand, the conduction behavior observed in the OFF state went after the space-charge-limited conduction composed of an ohmic region ($I \sim V$), a transition region ($I \sim V^2$), and a region of sharply

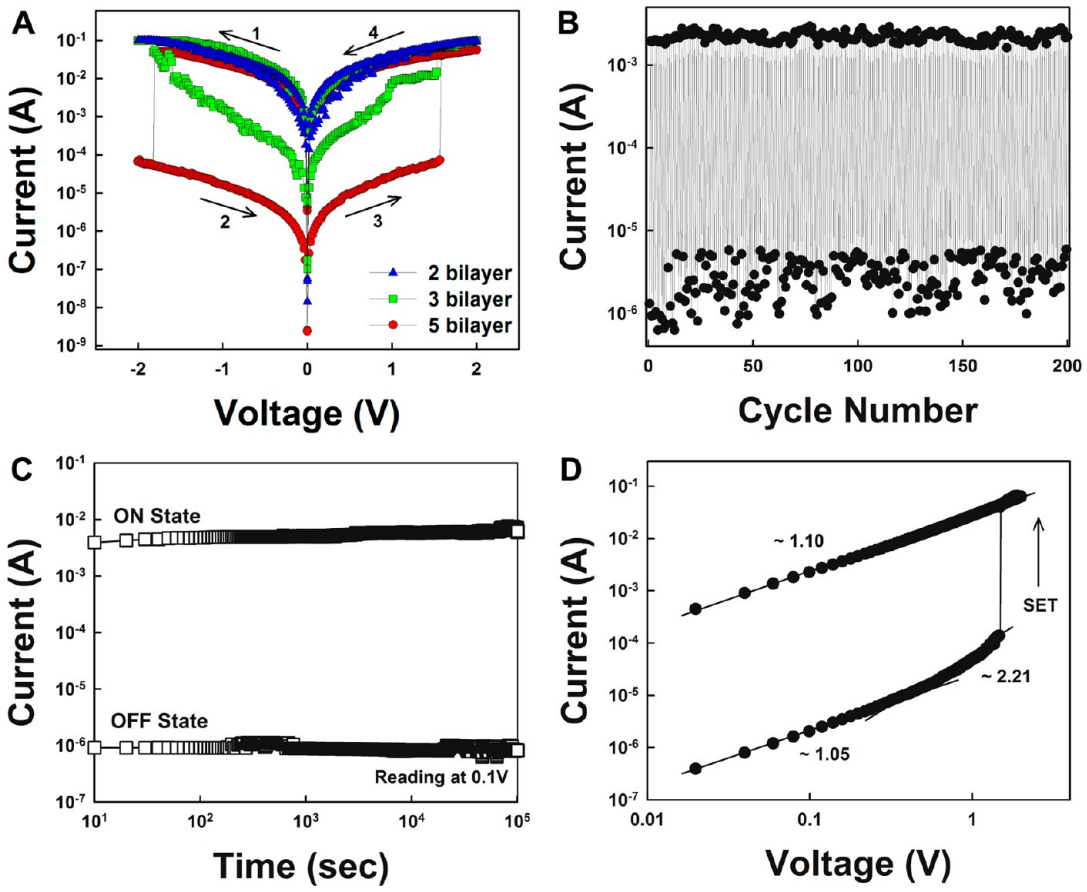

Figure 6. (A) *I*−*V* curves of the $(NH_2$-dendrimer/OA-BTO NP$)_n$ multilayer devices measured from 50 μm Ag electrodes with an increasing number of bilayers (*n*) ranging from 2 to 5. (B) Cycling and (C) retention time tests of the $(NH_2$-dendrimer/OA-BTO NP$)_5$ multilayer devices using a reading voltage of +0.1 V. (D) Linear fitting of the *I*−*V* curve for a five-bilayered device plotted on a log−log scale for the SET process during a positive voltage sweep.

increasing current.[40,72] These phenomena exactly coincided with those of the $(NH_2$-dendrimer/OA-$Fe_3O_4)_n$ multilayer-based devices that were previously reported by our group.[40]

Although the switching mechanism for ferroelectric perovskite-type memory devices is reportedly based on the intrinsic switching of ferroelectric domains,[73] the high-conductivity state—similar to the metallic ON state under the applied dc voltage sweep—cannot be explained by the switching mechanism based on ferroelectric polarization under a poling pulse. A possible mechanism can be proposed for the $(NH_2$-dendrimer/OA-BTO NP$)_n$ multilayer-based devices in our system based on the memristive model that has primarily been used to explain the resistive switching properties of transition metal oxide thin films or nanotubes.[58,70] As indicated by the XPS data in Figure 3, the OA-BTO NPs embedded in the LbL nanocomposite films contain a large quantity of Ti^{3+} with an oxygen vacancy state. These positively charged oxygen vacancies in the 8 nm OA-BTO lattices are repelled or attracted from the top electrode according to the electric field and can drift due to tunneling through a thin residual region (*i.e.*, organic layers below approximately 1 nm thickness per bilayer, including OA stabilizers and NH_2-dendrimer layers). This relationship significantly affects the electronic barrier to electron transport at the interface between the electrode and the multilayers. Therefore, a negative voltage applied to the top electrode attracts the positively charged carriers in the OA-BTO NP lattices. These charges drift in the electric field through the most favorable diffusion paths to form channels with high electrical conductivity.

These conductive channels can be confirmed using current-sensing atomic force microscopy (CS-AFM) (see Supporting Information, Figure S10). For the CS-AFM measurements, the $(NH_2$-dendrimer/OA-BTO NP$)_5$ multilayer film was deposited onto Pt-coated substrates, and an electrochemically inert Pt CS-AFM tip with a contact area of approximately 30 nm replaced the 50 μm Ag electrode as the top electrode. In this case, randomly distributed paths formed in the ON state as measured from the *I*−*V* curve of the five-bilayered NH_2-dendrimer/OA-BTO NP films. That is, once a large amount of conductive paths are formed, the conductive state of the device is converted to the ON state. However, when a reverse voltage is applied to the Pt tip electrode, the positively charged carriers in

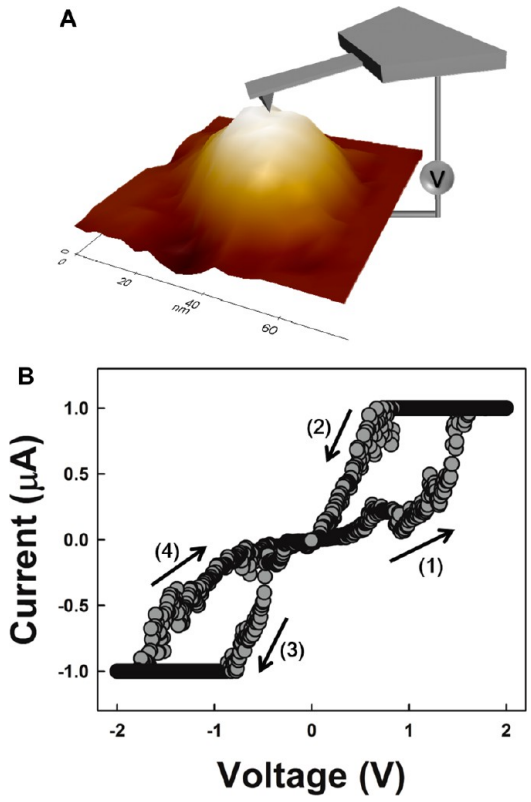

Figure 7. (A) Schematic diagram and (B) *I*−*V* curve of one bare OA-BTO NP measured using Pt.

the conducting paths are repelled from the Pt tip interface, and the initial electronic barrier is recovered again.[40,70] As a result, the conductive channels rupture in the OFF state. This switching mechanism is supported by the previous reports that both the time-dependent capacitance and the time-dependent resistance in the memristive model could be induced from the Fe^{2+} and Fe^{3+} with different mobilities in the 7 nm Fe_3O_4 NP lattices.[38]

For another switching mechanism, solid electrolytes sandwiched between a Ag (or a Cu) anode and an inert cathode were recently reported to cause bipolar switching *via* an electrochemical redox reaction based on the high mobility of Ag ions.[69,71,72] Furthermore, metal ion diffusion from the top electrode can form localized conductive channels that bridge the electrode materials under an electric field. However, our device displayed similar bipolar switching phenomena with electrochemically inert top electrodes such as Au, Pt, and W (see Supporting Information, Figure S11), which suggests that the redox reaction based on the electrochemically active Ag electrode is not closely related to the switching mechanism of the ligand addition-induced LbL NH_2-dendrimer/OA-BTO NP multilayers.

On the basis of these results, we investigated the possibility that one bare OA-BTO NP without any coated NH_2-dendrimer could operate as a nanoscale memory device (Figure 7A). For this investigation, OA-BTO NP-coated substrates were prepared on Pt-coated Si substrates using an extremely dilute 1.0×10^{-4} mg·mL^{-1} OA-BTO NP solution. The nonvolatile memory properties of one OA-BTO NP in a 70×70 nm^2 area were measured using a electrically inert Pt CS-AFM-tip electrode with a current compliance of 1.0 μA. As indicated in Figure 7B, one OA-BTO NP exhibited typical bipolar switching behavior.

CONCLUSION

We have reported for the first time the ability of LbL-assembled multilayers composed of highly monodisperse OA-BTO NPs with sub-10-nm dimensions to control the ferroelectric and resistive switching properties depending on the applied electric field. The high affinity between the amine groups on the NH_2-dendrimer and the Ti ions in the OA-BTO NPs allowed vertical growth of the (NH_2-dendrimer/OA-BTO NP)$_n$ multilayers in organic media without replacing the OA ligands. These results indicate that our approach (*i.e.*, ligand addition-induced LbL assembly) can be effectively used to prepare perovskite NP-based nanocomposite films. Additionally, the resulting multilayer films were found to have ferroelectric properties with reversible spontaneous polarization due to the respective OA-BTO NPs. Furthermore, bipolar resistive switching memory devices composed of the (NH_2-dendrimer/OA-BTO NP)$_n$ multilayers with ferroelectric properties displayed reliable memory performance (*i.e.*, ON/OFF current ratio $\sim 10^4$, low operating voltage <2 V and good endurance). In a future publication, we will focus on the preparation of LbL-assembled BTO NPs multilayers with improved ferroelectric and piezoelectric properties for high-performance electronics.

METHODS

Synthesis of 8-nm-Sized OA-BTO NPs. The synthetic procedure of 8-nm-sized OA-BTO NPs was modified from that of 20-nm-sized BTO NPs proposed by Dang *et al.*[51] First, titanium bis-(ammonium lactate) dihydroxide (1.2 mmol, 0.3534 g) was added to an aqueous solution (24 mL) containing barium hydroxide octahydrate (1.2 mmol, 0.3786 g). Then, 5 M NaOH solution (5 mL), oleic acid (8.4 mmol, 2.3726 g), and *tert*-butylamime (14.4 mmol, 1.0532 g) were sequentially added to the reaction mixture under magnetic stirring. The mixture was subsequently transferred to 30 mL Teflon-lined stainless steel autoclave. The sealed autoclave was mechanically stirred at 210 °C for 72 h. The resulting solution was centrifuged (8000 rpm, 10 min) three times with excess ethanol to remove the surfactant residuals. The precipitated white product was then dispersed in toluene or hexane (40 mL). Then, the centrifugation process (1000 rpm, 2 min) was repeated three times to remove the precipitates.

Build-up of LbL-Assembled Multilayers. The concentrations of OA-BTO NPs in toluene and NH_2-dendrimer in ethanol were adjusted to 10 and 2 mg·mL^{-1}. Quartz or silicon substrates were washed with an RCA solution ($H_2O/NH_3/H_2O_2$ = 5:1:1 v/v/v).

The substrates were first dipped in an ethanol solution of NH_2-dendrimers for 10 min, followed by washing twice with ethanol and drying with a gentle stream of nitrogen. The NH_2-dendrimer-coated substrates were then dipped into a toluene dispersion of OA-BTO NPs for 20 min, followed by washing with toluene and drying with a gentle stream of nitrogen. This process was repeated until the desired number of layers was deposited.

Transmission Measurement of LbL-Assembled Multilayers. Transmission of five-bilayered NH_2-dendrimer/OA-BTO NP multilayers on quartz glass was measured using a Perkin-Elmer Lambda 35 UV−vis spectrometer.

Fourier Transform Infrared Spectroscopy. Vibrational spectra were measured by Fourier transform infrared spectroscopy (iS10 FTIR, Thermo Fisher) in the absorbance and attenuated total reflection modes. The sample chamber was purged with N_2 gas for 2 h to eliminate water and CO_2 prior to conducting the FT-IR measurement. An ATR-FT-IR spectrum for the (NH_2-dendrimer/OA-BTO NP)$_n$ film deposited onto a Au-coated substrate was obtained from 300 scans with an incident angle of 80°. The acquired raw data were plotted after baseline correction, and the spectrum was smoothed using spectrum analyzing software (OMNIC, Nicolet).

Raman Spectroscopy. Raman spectra at room temperature were measured using a LabRam ARAMISS Raman spectroscopy system (Horiba Jobin-Yvon) using the 633 nm line of a He−Ne laser.

High-Resolution Transmission Electron Microscope. High-resolution transmission electron microscopy (HR-TEM, JEOL JEM 3000F microscope) was carried out on as-synthesized OA-BTO NPs.

Field-Emission Scanning Electron Microscope. The cross-sectional images of (NH_2-dendrimer/OA-BTO NP)$_n$ multilayer films were characterized by a field-emission scanning electron microscope (Hitachi S-4300).

X-ray Diffraction Measurement. Crystal structures of OA-BTO NP powder were examined using X-ray diffraction at room temperature. Data collection was performed in the 2θ range from 15° to 60° using Cu Kα radiation (λ = 1.54 Å, model: Bruker D8 Discover, Germany).

X-ray Photoelectron Spectroscopy Measurement. XPS spectra for the binding state of Ba and Ti ions were obtained using an AXIS-His spectrometer with monochromatic Mg Kα radiation (1253.6 eV). The survey spectra were recorded in the range 0−1200 eV with a constant pass energy of 20 eV; the high-resolution spectra were recorded with a constant pass energy of 20 eV. The X-ray source was run at a reduced power of 150 W. The pressure in the analysis chamber was maintained at 5×10^{-9} Pa for measurement. The Ar ion milling for NH_2-dendrimer/OA-BTO NP multilayer films was not used for XPS measurement.

Quartz Crystal Microgravimetry (QCM). A QCM device (QCM200, SRS) was used to examine the mass of the material deposited after each adsorption step. The resonance frequency of the QCM electrodes was approximately 5 MHz. The adsorbed mass of NH_2-dendrimers and OA-BTO NPs, Δm, was calculated from the change in QCM frequency, ΔF, using the Sauerbrey equation:

$$\Delta F(\mathrm{Hz}) = -56.6\Delta m_A$$

ΔF (Hz) = $-56.6\Delta m_A$, where Δm_A is the mass change per quartz crystal unit area in $\mu g \cdot cm^{-2}$.

Measurements of Polarization−Electric Field (P−E) Curve. Ferroelectric properties of (NH_2-dendrimer/OA-BTO NP)$_n$ multilayers sandwiched between top Au and bottom Pt electrodes were evaluated using a ferroelectric test system (Radiant Technologies, Inc., P-LC100) at 1 kHz and at room temperature.

Atomic Force Microscopy (AFM) Measurements. Topographic images for the confirmation of film roughness were acquired under tapping mode (Park Systems, XE-100) using a noncontact AFM tip. Additionally, the ferroelectric domain within the OA-BTO NPs was investigated by dynamic contact electrostatic force microscopy (Park Systems, XE-100) equipped with a lock-in amplifier (Park Systems, SR830). Furthermore, the conductive channels on the scale of nanometers were confirmed using current-sensing atomic force microscopy (Park Systems, XE-100) in contact mode with conductive tips.

Fabrication of Resistive Switching Nonvolatile Memory Devices. All samples were prepared on Si substrates (2 cm × 2 cm) with a SiO_2 layer of approximately 100 nm. A 30-nm-thick Ti layer was then deposited on the substrates, and a bottom electrode (Pt) was deposited by dc-magnetron sputtering. NH_2-dendrimer/OA-BTO NP multilayer films were then formed on the Pt-coated Si substrates. The resulting multilayer films were used without any thermal treatment. Top electrodes (Ag) of 50-μm-diameter thickness were then deposited onto the nanocomposite films. Pt or tungsten was also used as the top electrode instead of Ag for comparison. To examine the resistive switching behavior of the LbL multilayered devices, the current−voltage (I−V) curves were measured using a semiconductor parametric analyzer (Agilent 4155B) under ambient conditions. The pulsed voltage duration dependence of the high and low current states was examined using a semiconductor parametric analyzer (HP 4155A) and a pulse generator (Agilent 81104A).

Conflict of Interest: The authors declare no competing financial interest.

Acknowledgment. This work was supported by an NRF grant funded by the Ministry of Science, ICT & Future Planning (MSIP) (2010-0029106) and by the Human Resources Development Program of KETEP grant (20114010203050) funded by the Korea Government Ministry of Trade, Industry and Energy. This work was also supported by Samsung Research Funding Center for Future Technology (SRFC-MA1301-07).

Supporting Information Available: The particle size distribution of OA-BTO NPs, the FT-IR spectra and transmission curves of films, the QCM data, the AFM images of multilayers, and I−V curves of multilayer devices. This material is available free of charge *via* the Internet at http://pubs.acs.org.

REFERENCES AND NOTES

1. Hippel, A. V.; Breckenridge, R. G.; Chesley, F. G.; Tisza, L. High Dielectric Constant Ceramics. *Ind. Eng. Chem. Res.* **1946**, *38*, 1097–1109.
2. Matthias, B. T. Ferroelectricity. *Science* **1951**, *113*, 591–596.
3. Distler, G. I.; Konstantinova, V. P.; Gerasimov, Y. M.; Tolmacheva, G. A. Interaction of Defect and Domain Structures of Triglycine Sulphate Crystals in Ferroelectric and Paraelectric States. *Nature* **1968**, *218*, 762–765.
4. Westphal, W. B.; Mitsui, T. Dielectric and X-Ray Studies of $Ca_xBa_{1-x}TiO_3$ and $Ca_xSr_{1-x}TiO_3$. *Phys. Rev.* **1961**, *124*, 1354–1359.
5. Urban, J. J.; Yun, W. S.; Gu, Q.; Park, H. Synthesis of Single-Crystalline Perovskite Nanorods Composed of Barium Titanate and Strontium Titanate. *J. Am. Chem. Soc.* **2002**, *124*, 1186–1187.
6. Yun, W. S.; Urban, J. J.; Gu, Q.; Park, H. Ferroelectric Properties of Individual Barium Titanate Nanowires Investigated by Scanned Probe Microscopy. *Nano Lett.* **2002**, *2*, 447–450.
7. Ahn, C. H.; Rabe, K. M.; Triscone, J.-M. Ferroelectricity at the Nanoscale: Local Polarization in Oxide Thin Films and Heterostructures. *Science* **2004**, *303*, 488–491.
8. Fong, D. D.; Stephenson, G. B.; Streiffer, S. K.; Eastman, J. A.; Auciello, O.; Fuoss, P. H.; Thompson, C. Ferroelectricity in Ultrathin Perovskite Films. *Science* **2004**, *304*, 1650–1653.
9. Dicken, M. J.; Sweatlock, L. A.; Pacifici, D.; Lezec, H. J.; Bhattacharya, K.; Atwater, H. A. Electrooptic Modulation in Thin Film Barium Titanate Plasmonic Interferometers. *Nano Lett.* **2008**, *8*, 4048–4052.
10. Ionescu, A. M. Nanoelectronics: Ferroelectric Devices Show Potential. *Nat. Nanotechnol.* **2012**, *7*, 83–85.
11. Spanier, J. E.; Kolpak, A. M.; Urban, J. J.; Grinberg, I.; Ouyang, L.; Yun, W. S.; Rappe, A. M.; Park, H. Ferroelectric Phase Transition in Individual Single-Crystalline $BaTiO_3$ Nanowires. *Nano Lett.* **2006**, *6*, 735–739.
12. Kim, P.; Doss, N. M.; Tillotson, J. P.; Hotchkiss, P. J.; Pan, M.-J.; Marder, S. R.; Li, J.; Calame, J. P.; Perry, J. W. High Energy Density Nanocomposites Based on Surface-Modified $BaTiO_3$ and a Ferroelectric Polymer. *ACS Nano* **2009**, *3*, 2581–2592.

13. Yang, K.; Huang, X.; Huang, Y.; Xie, L.; Jiang, P. Fluoro-Polymer@$BaTiO_3$ Hybrid Nanoparticles Prepared *via* RAFT Polymerization: Toward Ferroelectric Polymer Nanocomposites with High Dielectric Loss for Energy Storage Application. *Chem. Mater.* **2013**, *25*, 2327–2388.
14. Schroeder, R.; Majewski, L. A.; Grell, M. High Performance Organic Transistors Using Solution-Processed Nanoparticle-Filled High-*k* Polymer Gate Insulators. *Adv. Mater.* **2005**, *17*, 1535–1539.
15. Kim, P.; Jones, S. C.; Hotchkiss, P. J.; Haddock, J. N.; Kippelen, B.; Marder, S. R.; Perry, J. W. Phosphonic Acid-Modified Barium Titanate Polymer Nanocomposites with High Permittivity and Dielectric Strength. *Adv. Mater.* **2007**, *19*, 1001–1005.
16. Son, J. Y.; Lee, J.-H.; Song, S.; Shin, Y.-H.; Jang, H. M. Four-States Multiferroic Memory Embodied Using Mn-Doped $BaTiO_3$ Nanorods. *ACS Nano* **2013**, *7*, 5522–5529.
17. O'Brien, S.; Brus, L.; Murray, C. B. Synthesis of Monodisperse Nanoparticles of Barium Titanate: Toward a Generalized Strategy of Oxide Nanoparticle Synthesis. *J. Am. Chem. Soc.* **2001**, *123*, 12085–12086.
18. Niederberger, M.; Pinna, N.; Polleux, J.; Antonietti, M. A General Soft-Chemistry Route to Perovskites and Related Materials: Synthesis of $BaTiO_3$, $BaZrO_3$, and $LiNbO_3$ Nanoparticles. *Angew. Chem., Int. Ed.* **2004**, *43*, 2270–2273.
19. Nuraje, N.; Su, K.; Haboosheh, A.; Samson, J.; Manning, E. P.; Yang, N.-L.; Matsui, H. Room Temperature Synthesis of Ferroelectric Barium Titanate Naoparticles Using Peptide Nanorings as Templates. *Adv. Mater.* **2006**, *18*, 807–811.
20. Liu, H.; Hu, C.; Wang, Z. L. Composite-Hydroxide-Mediated Approach for the Synthesis of Nanostructures of Complex Functional-Oxides. *Nano Lett.* **2006**, *6*, 1535–1540.
21. Morerira, M. L.; Mambrini, G. P.; Volanti, D. P.; Leite, E. R.; Orlandi, M. O.; Pizani, P. S.; Mastelaro, V. R.; Paiva-Santos, C. O.; Longo, E.; Varela, J. A. Hydrothermal Microwave: A New Route to Obtain Photoluminescent Crystalline $BaTiO_3$ Nanoparticles. *Chem. Mater.* **2008**, *20*, 5381–5387.
22. Demirörs, A. F.; Imhof, A. $BaTiO_3$, $SrTiO_3$, $CaTiO_3$, and $Ba_xSr_{1-x}TiO_3$ Particles: A General Approach for Monodisperse Colloidal Perovskites. *Chem. Mater.* **2009**, *21*, 3002–3007.
23. Adireddy, S.; Lin, C.; Cao, B.; Zhou, W.; Caruntu, G. Solution-Based Growth of Monodisperse Cube-Like $BaTiO_3$ Colloidal Nanocrystals. *Chem. Mater.* **2010**, *22*, 1946–1948.
24. Polking, M. J.; Han, M.-G.; Yourdkhani, A.; Petkov, V.; Kisielowski, C. F.; Volkov, V. V.; Zhu, Y.; Caruntu, G.; Alivisatos, A. P. Ferroelectric Order in Individual Nanometre-Scale Crystals. *Nat. Mater.* **2012**, *11*, 700–709.
25. Subodh, G.; Deepu, V.; Mohanan, P.; Sebastian, M. T. Dielectric Response of High Permittivity Polymer Ceramic Composite with Low Loss Tangent. *Appl. Phys. Lett.* **2009**, *95*, 062903.
26. Zhang, X.; Wei, S.; Haldolaarachchige, N.; Colorado, H. A.; Luo, Z.; Young, D. P.; Guo, Z. Magnetoresistive Conductive Polyaniline-Barium Titanate Nanocomposites with Negative Permittivity. *J. Phys. Chem.* **2012**, *116*, 15731–15740.
27. Decher, G. Fuzzy Nanoassemblies: Toward Layered Polymeric Multicomposites. *Science* **1997**, *277*, 1232–1237.
28. Caruso, F.; Caruso, R. A.; Möhwald, H. Nanoengineering of Inorganic and Hybrid Sphere by Colloidal Templating. *Science* **1998**, *282*, 1111–1114.
29. Podsiadlo, P.; Kaushik, A. K.; Arruda, E. M.; Waas, A. M.; Shim, B. S.; Xu, J. D.; Nandivada, H.; Pumplin, B. G.; Lahann, J.; Ramamoorthy, A.; *et al*. Ultrastrong and Stiff Layered Polymer Nanocomposites. *Science* **2007**, *318*, 80–83.
30. Jiang, C.; Markutsya, S.; Pikus, Y.; Tsukruk, V. V. Freely Suspended Nanocomposite Membranes as Highly Sensitive Sensors. *Nat. Mater.* **2004**, *3*, 721–728.
31. Lee, S. W.; Kim, J.; Chen, S.; Hammond, P. T.; Shao-Horn, Y. Carbon Nanotube/Manganese Oxide Ultrathin Film Electrodes for Electrochemical Capacitors. *ACS Nano* **2010**, *4*, 3889–3896.
32. Lee, D.; Rubner, M. F.; Cohen, R. E. All-Nanoparticle Thin-Film Coatings. *Nano Lett.* **2006**, *6*, 2305–2312.
33. Suck, G. K.; Quinn, J. F.; Quinn, A.; Caruso, F. Assembly of Ultrathin Polymer Multilayer Films by Click Chemistry. *J. Am. Chem. Soc.* **2006**, *128*, 9318–9319.
34. Wen, K.; Maoz, R.; Cohen, H.; Sagiv, J.; Gibaud, A.; Desert, A.; Ocko, B. M. Postassembly Chemical Modification of a Highly Ordered Organosilane Multilayer: New Insights into the Structure, Bonding, and Dynamics of Self-Assembling Silane Monolayers. *ACS Nano* **2008**, *2*, 579–599.
35. Chan, E. W. L.; Lee, D.-C.; Ng, M.-K.; Wu, G.; Lee, K. Y. C.; Yu, L. A Novel Layer-by-Layer Approach to Immobilization of Polymers and Nanoclusters. *J. Am. Chem. Soc.* **2002**, *124*, 12238–12243.
36. Leibowitz, F. L.; Zheng, W.; Maye, M. M.; Zhong, C.-J. Structures and Properties of Nanoparticle Thin Films Formed *via* a One-Step Exchange-Cross-Linking-Precipitation Route. *Anal. Chem.* **1999**, *71*, 5076–5083.
37. Lee, B.; Kim, Y.; Lee, S.; Kim, Y. S.; Wang, D.; Cho, J. Layer-by-Layer Growth of Polymer/Quantum Dot Composite Multilayers by Nucleophilic Substitution on Organic Media. *Angew. Chem., Int. Ed.* **2010**, *49*, 359–363.
38. Kim, Y.; Lee, C.; Shim, I.; Wang, D.; Cho, J. Nucleophilic Substitution Reaction Based Layer-by-Layer Growth of Superparamagnetic Nanocomposite Films with High Nonvolatile Memory Performance. *Adv. Mater.* **2010**, *22*, 5140–5144.
39. Yoon, M.; Kim, Y.; Cho, J. Multifunctional Colloids with Optical, Magnetic, and Superhydrophobic Properties Derived from Nucleophilic Substitution-Induced Layer-by-Layer Assembly in Organic Media. *ACS Nano* **2011**, *5*, 5417–5426.
40. Ko, Y.; Baek, H.; Kim, Y.; Yoon, M.; Cho, J. Hydrophobic Nanoparticle-Based Nanocomposite Films Using *In Situ* Ligand Exchange Layer-by-Layer Assembly and Their Nonvolatile Memory Applications. *ACS Nano* **2013**, *7*, 143–153.
41. Ko, Y.; Baek, H.; Kim, Y.; Yoon, M.; Cho, J. Correction to Hydrophobic Nanoparticle-Based Nanocomposite Films Using *in Situ* Ligand Exchange Layer-by-Layer Assembly and Their Nonvolatile Memory Applications. *ACS Nano* **2013**, *7*, 11445–11445.
42. Kim, D.; Kim, Y.; Cho, J. Solvent-Free Nanocomposite Colloidal Fluids with highly Integrated and Tailored Functionalities: Rheological, Ionic Conduction, and Magneto-Optical Properties. *Chem. Mater.* **2013**, *25*, 3834–3843.
43. Lee, S.; Lee, B.; Kim, B. J.; Park, J.; Bae, W. K.; Char, K.; Hawker, C. J.; Bang, J.; Cho, J. Free-Standing Nanocomposite Multilayers with Various Length-Scales, Adjustable Internal Structures and Functionalities. *J. Am. Chem. Soc.* **2009**, *131*, 2579–2587.
44. Ejima, H.; Richardson, J. J.; Liang, K.; Best, J. P.; Koeverden, M. P.; Such, G. K.; Cui, J.; Caruso, F. One-Step Assembly of Coordination Complexes for Versatile Film and Particle Engineering. *Science* **2013**, *341*, 154–157.
45. Hong, J.; Bae, W.; Oh, S.; Lee, H.; Char, K.; Caruso, F.; Cho, J. Tunable Superhydrophobic and Optical Properties of Colloidal Films Coated with Block Copolymer Micelle/Micelle Multilayers. *Adv. Mater.* **2007**, *19*, 4364–4369.
46. Cho, J.; Hong, J.; Char, K.; Caruso, F. Nanoporous Block Copolymer Micelle/Micelle Multilayer Films with Dual Optical Properties. *J. Am. Chem. Soc.* **2006**, *128*, 9935–9942.
47. Cho, J.; Char, K.; Hong, J.-D.; Lee, K.-B. Fabrication of Highly Ordered Multilayer Films Using Spin Self-Assembly Method. *Adv. Mater.* **2001**, *13*, 1076–1078.
48. Cho, J.; Char, K. Effect of Layer Integrity of Spin-Assembled Multilayer Films on Surface Wettability. *Langmuir* **2004**, *20*, 4011–4015.
49. Ariga, K.; Yamauchi, Y.; Rydzek, G.; Ji, Q.; Yonamine, Y.; Wu, K. C.-W.; Hill, J. P. Layer-by-Layer Nanoarchitectonics: Invention, Innovation, and Evolution. *Chem. Lett.* **2014**, *43*, 36–68.
50. Dierendonck, M.; Koker, S. D.; Rycke, R. D.; Geest, B. G. D. Just Spray It - LbL Assembly Enters a New Age. *Soft Matter* **2014**, *10*, 804–807.
51. Dang, F.; Mimura, K.; Kato, K.; Imai, H.; Wada, S.; Haneda, H.; Kuwabara, M. *In Situ* Growth $BaTiO_3$ Nanocubes and Their Superlattice from an Aqueous Process. *Nanoscale* **2012**, *4*, 1344–1349.
52. Jiang, G.; Baba, A.; Advincula, R. Nanopattering and Fabrication of Memory Devices from Layer-by-Layer Poly(3,4-ethylenedioxythiophene)-Poly(styrene sulfonate) Ultrathin Films. *Langmuir* **2007**, *23*, 817–825.

53. Das, B. C.; Batabyal, S. K.; Pal, A. J. A Bit per Particle: Electrostatic Assembly of CdSe Quantum Dots as Memory Elements. *Adv. Mater.* **2007**, *19*, 4172–4176.
54. DiDomenico, M.; Wemple, S. H.; Porto, S. P. S.; Bauman, R. P. Raman Spectrum of Single-Domain $BaTiO_3$. *Phys. Rev.* **1968**, *174*, 522–530.
55. Busca, G.; Ramis, G.; Amores, J. M. G.; Escribano, V. S.; Piaggio, P. FT Raman and FTIR Studies of Titanias and Metatitanate Powders. *J. Chem. Soc., Faraday Trans.* **1994**, *90*, 3181–3190.
56. Smith, M. B.; Page, K.; Siegrist, T.; Redmond, P. L.; Walter, E. C.; Seshadri, R.; Brus, L. E.; Steigerwald, M. L. Crystal Structure and the Paraelectric-to-Ferroelectric Phase Transition of Nanoscale $BaTiO_3$. *J. Am. Chem. Soc.* **2008**, *130*, 6955–6963.
57. Barman, S.; Deng, F.; McCreery, R. C. Conducting Polymer Memory Devices Based on Dynamic Doping. *J. Am. Chem. Soc.* **2008**, *130*, 11073–11081.
58. Yang, J. J.; Pickett, M. D.; Li, X.; Ohlberg, D. A. A.; Stewart, D. R.; Williams, R. S. Memrisitve Switching Mechanism for Metal/Oxide/Metal Nanodevices. *Nat. Nanotechnol.* **2008**, *3*, 429–433.
59. Sathish, M.; Viswanathan, B.; Viswanath, R. P.; Gopinath, C. S. Synthesis, Characterization, Electronic Structure, and Photocatalytic Activity of Nitrogen-Doped TiO_2 Nanocatalyst. *Chem. Mater.* **2005**, *17*, 6349–6353.
60. Martínez-Ferrero, E.; Sakatani, Y.; Boissière, C.; Grosso, D.; Fuertes, A.; Fraxedas, J.; Sanchez, C. Nanostructured Titanium Oxynitride Porous Thin Films as Efficient Visible-Active Photocatalysts. *Adv. Funct. Mater.* **2007**, *17*, 3348–3354.
61. Kim, Y.; Han, H.; Kim, Y.; Lee, W.; Alexe, M.; Baik, S.; Kim, J. K. Ultrahigh Density Array of Epitaxial Ferroelectric Nanoislands on Conducting Substrates. *Nano Lett.* **2010**, *10*, 2141–2146.
62. Lisinski, S.; Schaniel, D.; Ratke, L.; Woike, T. Second-Harmonic Generation by Ferroelectric Microparticles in Aerogels. *Chem. Mater.* **2006**, *18*, 1534–1538.
63. Becker, K.-D.; Schrader, M.; Kwon, H.-S.; Yoo, H.-I. Electrical and Optical Characterization of Undoped $BaTiO_3$ in the Quenched State. *Phys. Chem. Chem. Phys.* **2009**, *11*, 3082–3089.
64. Mimura, K.-I.; Hiramatsu, K.; Sakamoto, W.; Yogo, T. Ferroelectric Properties of Alkoxy-Derived Transparent $BaTiO_3$ Nanoparticles/Polymer Hybrid. *Mater. Lett.* **2012**, *89*, 40–42.
65. Lee, J.-K.; Hong, K.-S.; Jang, J.-W. Roles of Ba/Ti Ratios in the Dielectric Properties of $BaTiO_3$ Ceramics. *J. Am. Ceram. Soc.* **2001**, *84*, 2001–2006.
66. Junquera, J.; Ghosez, P. Critical Thickness for Ferroelectricity in Perovskite Ultrathin Films. *Nature* **2003**, *422*, 506–509.
67. Zhou, Z.; Lin, Y.; Tang, H.; Sodano, H. A. Hydrothermal Growth of Highly Textured $BaTiO_3$ Films Composed of Nanowires. *Nanotechnology* **2013**, *24*, 095602.
68. Mandal, D.; Kim, K. J.; Lee, J. S. Simple Synthesis of Palladium Nanoparticles, ß-Phase Formation, and the Control of Chain and Dipole Orientations in Palladium-Doped Poly(vinylidene fluoride) Thin Films. *Langmuir* **2012**, *28*, 10310–10317.
69. Waser, R.; Aono, M. Nanoionics-Based Resistive Switching Memories. *Nat. Mater.* **2007**, *6*, 833–840.
70. Strukov, D. B.; Snider, G. S.; Stewart, D. R.; Williams, R. S. The Missing Memristor Found. *Nature* **2008**, *453*, 80–83.
71. Terabe, K.; Hasegawa, T.; Nakayama, T.; Aono, M. Quantized Conductance Atomic Switch. *Nature* **2005**, *433*, 47–50.
72. Yang, Y. C.; Pan, F.; Liu, Q.; Liu, M.; Zeng, F. Fully Room-Temperature-Fabricated Nonvolatile Resistive Memory for Ultrafast and High-Density Memory Application. *Nano Lett.* **2009**, *9*, 1636–1643.
73. Pantel, D.; Goetze, S.; Hesse, D.; Alexe, M. Room-Temperature Ferroelectric Resistive Switching in Ultrathin $Pb(Zr_{0.2}Ti_{0.8})O_3$ Films. *ACS Nano* **2011**, *5*, 6032–6038.